Energy & Environmental Science

PAPER

View Article Online
View Journal | View Issue

Cite this: *Energy Environ. Sci.*, 2025, **18**, 9865

Solvent-additive cascade engineering enables single-oriented perovskite films with facet-driven performance and stability

Bo Zhou,[ab] Pei Zhao,[d] Junxue Guo,[ae] Shuaifeng Hu,[f] Xin Guo,[ab] Jiewei Liu*[a] and Can Li*[bc]

Received 31st July 2025,
Accepted 2nd October 2025

DOI: 10.1039/d5ee04415d

rsc.li/ees

Facet engineering is an important strategy for enhancing the efficiency and stability of perovskite devices. However, the formation of high-quality, tunable crystal facets remains a challenging endeavor. Here, we employed a novel solvent-additive cascade regulation (SACR) strategy to create homogenous orientations *via* a two-step method. Mechanistic analysis reveals that solvents drive orientation *via* topochemical assembly, while additives regulate specific facet growth through differential bonding intensities with crystal nuclei. With the SACR method, we successfully obtained perovskite films with homogeneous (111) and (100)-oriented facets following the Wulff construction rule. The resulting n–i–p structured devices achieved optimal efficiencies of 23.32% and 25.33%, respectively. Notably, the (100)-oriented devices exhibited superior photoelectric performance, whereas the (111)-oriented devices demonstrated better long-term stability. This work underscores the critical role of facet engineering in tailoring the optoelectronic properties and structural stability of perovskite films, offering a viable pathway toward efficient and durable perovskite solar cells.

Broader context

Perovskite solar cells (PSCs) hold great promise for next-generation photovoltaics, yet commercialization is limited by the trade-off between efficiency and stability. Facet engineering—controlling the crystallographic orientation of perovskite grains—offers a route to overcome this challenge, as different facets (*e.g.*, (100) and (111)) exhibit distinct charge transport and degradation behaviors. However, fabricating homogeneous single-orientation films remains difficult due to the intertwined roles of solvents and additives during crystallization. Here, we introduce a solvent–additive cascade regulation (SACR) strategy that sequentially couples solvent-driven intermediate assembly with additive-directed facet refinement. Using tailored solvent systems (DMF/DMSO or DMF/NMP) and specific additives (CHA or CHAI), we achieve near-perfect (111) or (100) single orientations, consistent with Wulff construction principles. Mechanistic studies reveal that solvents template the initial orientation, while additives enforce homogeneity through facet-selective bonding, effectively resolving orientation disorder in two-step films. This approach enables devices that simultaneously push performance boundaries: (100)-oriented PSCs reach a record PCE of 25.33%, while (111)-oriented counterparts retain over 95% of their efficiency after 2000 h of operation. These findings establish facet control as a unifying strategy to bridge efficiency and stability in PSCs.

Introduction

Perovskite solar cells (PSCs) have garnered significant attention due to their impressive power conversion efficiency (PCE).[1,2] The performance of these devices is closely linked to the quality of crystal facets in the active layer.[3] Common crystal growth methods often result in polycrystalline structures with random orientations, leading to electronic heterogeneity that reduces both PCE and stability.[4] However, a comprehensive understanding of the mechanisms and effective strategies for facet engineering, which is closely related to the complex growth dynamics involving intricate interactions between additives, precursor components and intermediate phases, remains elusive.

---

[a] *State Key Laboratory of Photoelectric Conversion and Utilization of Solar Energy, Dalian Institute of Chemical Physics, Chinese Academy of Sciences, Dalian 116023, China. E-mail: jwliu@dicp.ac.cn*
[b] *University of Chinese Academy of Sciences, Beijing 100049, China. E-mail: canli@dicp.ac.cn*
[c] *State Key Laboratory of Catalysis, Dalian Institute of Chemical Physics, Chinese Academy of Sciences, Dalian 116023, China*
[d] *Research Center for Computational Science, Institute for Molecular Science, Okazaki 444-8585, Japan*
[e] *School of Chemistry and Materials Science, University of Science and Technology of China, Hefei 230026, China*
[f] *Clarendon Laboratory, Department of Physics, University of Oxford, Parks Road, Oxford OX1 3PU, UK*

To date, most strategies for controlling facet orientation have focused on one-step methods, such as epitaxial growth,[5] template-assisted growth,[6] and manipulation of solvents and additives.[7] In contrast, there has been limited exploration of two-step processes, mainly due to their sequential deposition nature.[8] In our previous work, it was found that a ternary solvent mixture (DMF/DMSO/NMP) inherently promotes the formation of (111)-oriented perovskite films *via* a two-step method, even without additional additives.[9] This solvent-driven orientation regulation arises from the distinct coordination capabilities between solvent molecules and PbI_2 in the precursor, which influence the formation of intermediate solvent phases and subsequent growth kinetics of specific crystal facets. However, solvent regulation alone is insufficient. The solvent-induced disordering effect disrupts facet-selective nucleation due to the subsequent uncontrollable crystal growth triggered by solvent removal, leading to facet heterogeneity.[10]

To address the disordering effect, additives are typically required to enhance orientation. A common strategy employs long-chain organic ammonium salts (LOASs), typically by reducing the surface energy of the target facet to create a single orientation. LOASs are often preferentially adsorbed by low-index facets with low surface energy, which refers to the (100) facet rather than the (111) facet. This mechanism likely explains why previously reported (111)-dominated films contain noticeable (100) facet distributions[11] and thus cannot be considered uniformly oriented. Furthermore, while LOAS ligands are effective in the one-step method,[12] they fail to replicate the facet achievable in the two-step method,[13] where stepwise processing introduces unresolved mechanistic complexities. To address the research gap of two-step methods, it is necessary to explore new types of additives. As previously reported by the Park group,[14] high-quality perovskite films with (111) preferred orientation can be achieved with the cyclohexylamine (CHA) additive; similarly, (100)-oriented films can be obtained by adding the cyclohexylamine iodide (CHAI) additive.[15]

Nonetheless, how to simultaneously harness the orientation-directing effect of solvent coordination and additive–facet interaction within a single strategy remains unexplored, leaving a critical gap in achieving well-defined single orientation beyond the commonly observed preferred growth in two-step processed films. Considering that both solvents and additives have their own preferred orientation responses, it is essential to integrate the two factors in a coordinated manner to develop a new method for improving the reproducibility of single-oriented film fabrication. The Tang group,[16] through studying the aggregative luminescence (AIE) in perovskite precursors, identified two specific solvents—DMSO and NMP—based on the unique coordination capability between Pb^{2+} and solvents. Combined with our previous understanding of solvent effects, this work primarily focuses on comparing the DMF/DMSO and DMF/NMP solvent systems. After selectively introducing additives, we successfully prepared homogenous perovskite films with (111) and (100) orientations using the solvent-additive cascade regulation (SACR) strategy, by employing CHA and CHAI as additives in the DMF/DMSO and DMF/NMP systems, respectively. By manipulating the coordination of solvents and additives during the two-step deposition process, the results demonstrated that the choice of solvent and additive profoundly impacts orientation, leading to high-quality and tunable facets. Investigation of the two-step process revealed that solvents and additives function in two distinct stages: PbI_2 or NMP intermediate phases serve as growth templates and provide the core driving force for different dominant facets, while additives influence facet growth and mass transfer through varying interactions and bonding with the dominant facets. Following this, the facet-dependent properties of homogenous (111) and (100) facets can be analyzed and found that n–i–p structured devices made from (100)-oriented films achieved a higher PCE of 25.33%, while (111)-oriented films demonstrated superior long-term stability, maintaining $>95\%$ performance after 2000 hours under ambient conditions. This work not only uncovers the complex interplay among solvents, additives, and crystal growth, but also provides insights into the relationship between facet orientation and device performance, paving the way for the development of single-oriented perovskite films for various electronic applications.

Results and discussion

Impact of the SACR strategy on the perovskite orientation

(111)- and (100)-dominated perovskite films were obtained *via* the SACR strategy. Fig. 1a illustrates the SACR fabrication process, which involves dissolving the PbI_2 in different solvent systems during the first step and then spin-coating the additive solution onto the $FACsPbI_3$ films before annealing in the second step (Fig. S1). This strategy provides a reproducible approach for fabricating perovskite films with different preferred orientations *via* a two-step method.

The orientation of the resulting films was analyzed using grazing-incidence wide-angle X-ray scattering (GIWAXS) measurement. As shown in Fig. 1b and d, the GIWAXS patterns exhibit characteristic Debye–Scherrer rings corresponding to the cubic $FAPbI_3$-(100), (110), and (111) crystal planes at scattering vectors q of 10.0, 14.1, and 17.5 nm^{-1}, respectively.[17] (*hkl*) reflections along q_z indicate that the (*hkl*) planes are parallel to the substrate, confirming the (*hkl*) orientation. After identifying the diffraction patterns, it was found that the DMF/DMSO solvents favor the (111) orientation, while DMF/NMP solvents favor the (100) orientation, as evidenced by the corresponding highest XRD peaks (Fig. S4). Notably, the signals appear more as discrete ring (or arch)-like patterns due to a certain degree of structural disorder and misalignment with respect to the single orientation. Fig. 1b shows that in the DMF/DMSO solvent system, two main orientations of (100) and (200) diffraction arcs are detected for the films; Fig. 1d shows that in the DMF/NMP solvent system, although there are no significant (111) reflections, (100) and (200) reflections appear almost as rings. These pieces of evidence all indicate the existence of disordering effects induced by the solvents.

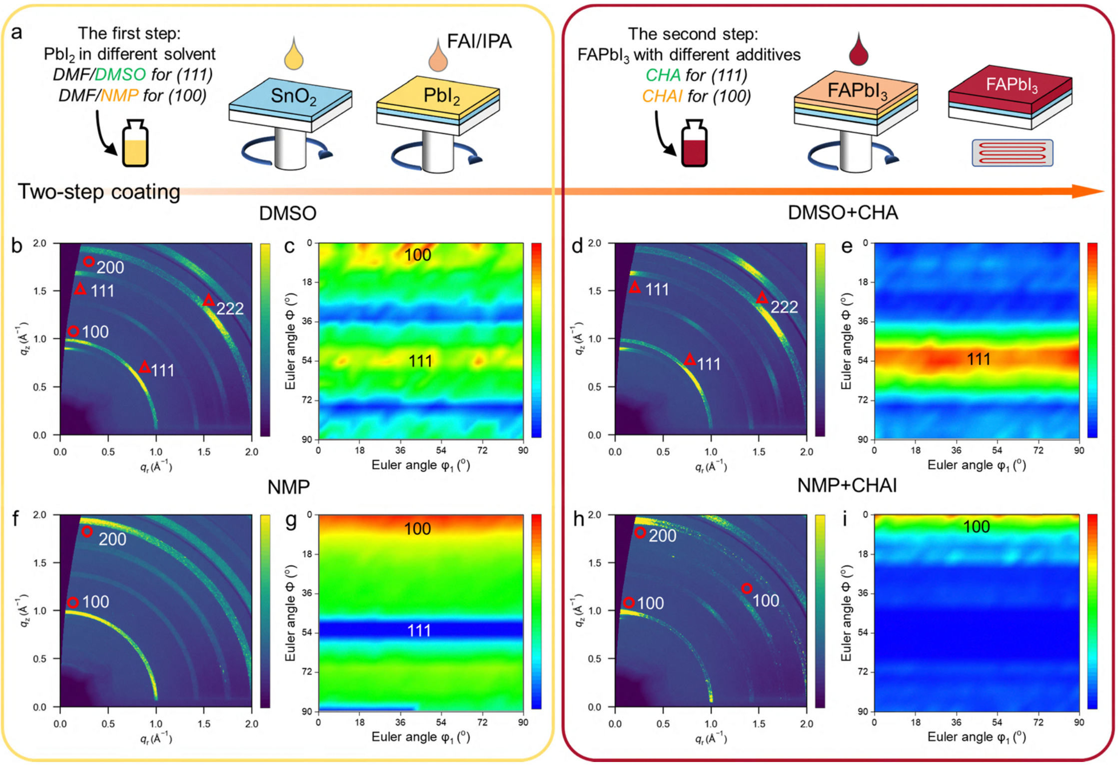

Fig. 1 (a) Schematic representation of the fabrication method for the solvent-additive cascade regulation (SACR) strategy. (b), (d), (f) and (h) GIWAXS and (c), (e), (g) and (i) ODF results of perovskite films prepared with different solvent systems without or with the SACR method.

When the additives CHA and CHAI are added, the GIWAXS pattern (Fig. 1f and h) drastically changes to bright scattering spots, revealing a switch from randomly disordered to highly ordered crystalline stacking. After integrating the azimuth of GIWAXS shown in Fig. S5 and S6, it was found that the bright (111) scattering spot is concentrated in the region of the azimuthal angle ≈90° (Fig. 1f) in the DMF/DMSO solvents, while the (100) facet is arranged at ≈54° relative to the (111) faces parallel to the substrate, indicating that almost all (111) faces in the film are arranged parallel to the substrate. Furthermore, the GIWAXS pattern in the DMF/NMP solvents exhibits the opposite alignment, with a (100) azimuthal angle of 90° and a (111) azimuthal angle of 54°. This angle matches the ideal crystallographic angle for perovskites, confirming the film's well-ordered stacking facets. Therefore, we successfully obtained perovskite films with (111) and (100) orientations, enabling further exploration of facet-dependent properties.

To ultimately confirm the single orientation of different samples, texture analysis was conducted using advanced inverse pole figure (IPF) orientation distribution function (ODF) investigation, with results presented in Fig. 1c, e, g and i. ODF is commonly used in materials science to describe the statistical distribution of crystal orientations. After obtaining pole figure (PF) data from polycrystalline thin films through X-ray diffraction, the three-dimensional spatial distribution can be reconstructed using the spherical harmonic expansion method or the maximum entropy method.[18] This enables the evaluation of the orientation uniformity and reveals the overall anisotropy of the perovskite film.[19] The ODF plots contain both the three Euler angles (φ_1, Φ, and φ_2) that describe the orientation information and the intensity information, directly reflecting the preferred orientations in the polycrystalline film and their degree of preference. Typically, ODF plots are sliced at φ_2 intervals of 5°, as shown in Fig. S8–S11. For ease of analysis, a $\varphi_2 = 45°$ slice is selected here, where the color scale in the slice represents the ODF density, indicating the strength of the texture.

By comparing the experimental ODFs with the Euler space coordinates, specific Euler angle regions of the films were investigated. The standard reference ODF patterns can be found in Fig. S7. Samples prepared with DMF/DMSO solvents exhibited two prominent regions ($\theta = 0°$, $\theta = 45°$), indicating a mixture of (111) and (100) orientations.[20] In contrast, samples prepared with DMF/NMP solvents displayed distribution across the entire range, with the highest ODF density near ($\theta = 0°$), suggesting a higher proportion of (100) facets with randomly oriented anisotropy. After SACR treatment, the reduction in the width of the ODF region confirms the improvement in orientation purity. Fig. 1e and i show the only specific Euler angle corresponding to the (111) and (100) orientations, respectively. The significant changes in ODFs demonstrate that the SACR strategy successfully optimized the texture uniformity of the film, enabling the identification of the dominant orientation. It is important to note that, as polycrystalline films, perovskite thin films exhibit fibre-textured characteristics, meaning that the sides facing each other are randomly distributed (φ_1 = any).

Understanding the mechanism of solvent influence on orientation

For the SACR strategy, the mechanism behind the preferred facet orientation should be related to both solvents and additives. First, the effect of different solvents on orientation is analyzed. With DMF/DMSO solvents, the parallel growth of the (111) facet on (001)PbI_2 based on the topochemical assembly mechanism has been well-documented in ref. 21. Typically, residual PbI_2 can be observed in the perovskite film, as shown in the XRD pattern in Fig. S4. As depicted in Fig. 2a, an almost perfect lattice match is observed. The HRTEM image shows the PbI_2(001) plane, which is parallel to the (111) facet of $FAPbI_3$, (as confirmed in Fig. S12). The crystallographic reason for this alignment is illustrated in the schematic diagram in Fig. 2a. The interplanar distance of the (001) plane of PbI_2 theoretically matches that of (111) × 2 of $FAPbI_3$, *i.e.*, $(111)_{FAPbI_3}//(001)_{PbI_2}$, which minimizes the misfit energy caused by the lattice difference between PbI_2 and $FAPbI_3$.

In DMF/NMP solvents, crystal growth follows an alternative pathway along a different coherent interface. GIWAXS analysis in the low 2θ range of 5–10° (Fig. 2c) reveals that even after annealing, perovskite films retain intermediate phase peaks related to the (120) planes of $MA_2(DMF)_2Pb_3I_8$, which aligns topologically with the (100) facet. This observation is consistent with the other study with DMF/DMSO solvents,[22] as demonstrated by the coincident selected area electron diffraction (SAED) patterns and the lattice match schematic of $MA_2(DMF)_2Pb_3I_8$ along the [012] axis and $FAPbI_3$ along the [111] axis shown in Fig. 2b. ODF analysis indicates that even before SCAR treatment, the DMF/NMP solvent system already

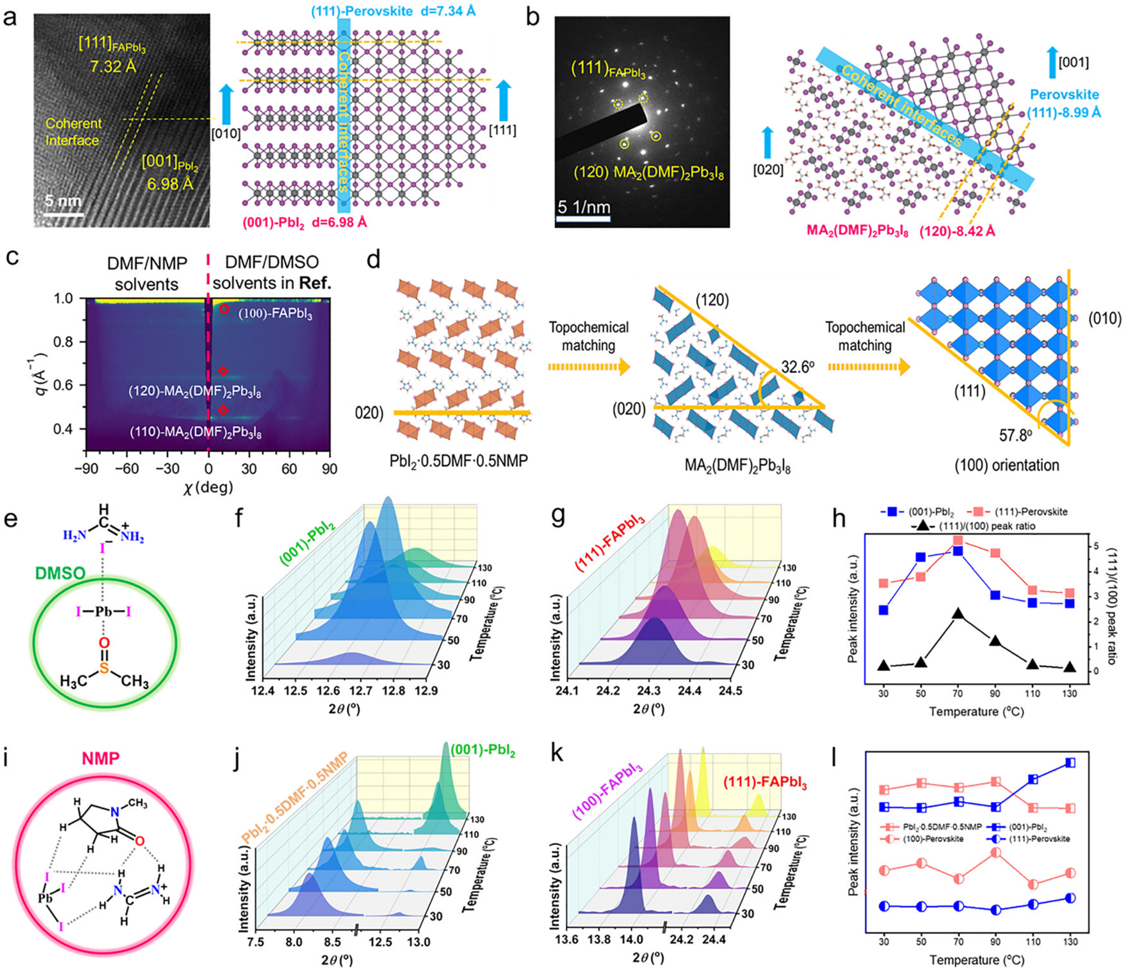

Fig. 2 (a) The HRTEM image and schematic illustration of the lattice matching between PbI_2 (001) and $FAPbI_3$ (111). (b) Selected area electron diffraction (SAED) pattern and schematic illustration of the lattice matching between $MA_2(DMF)_2Pb_3I_8$ along the [012] axis and $FAPbI_3$ along the [111] axis. (c) GIWAXS intensity maps following azimuth integral of DMF/NMP solvents compared to DMF/DMSO solvents in ref. 29. (d) The schematic illustration of topochemical matching and intermediate phases in DMF/NMP solvents. Schematic illustration of the interactions between solvents and perovskite species: (e) DMSO + PbI_2 + FAI, (i) NMP + PbI_2 + FAI. (f) XRD peaks of PbI_2 at a series of gradient temperatures after the first step for DMF/DMSO solvents, and (g) corresponding perovskite (111) peaks after the second step. (h) Analysis of peak intensity variations of (f) and (g) and the X-ray diffraction peak ratio of (111) to (100) at various annealing temperatures. (j) XRD peaks of the $PbI_2 \cdot 0.5DMF \cdot 0.5NMP$ intermediate phase and PbI_2 at a series of gradient temperatures after the first step for DMF/NMP solvents, and (k) corresponding perovskite (100) and (111) peaks after the second step. (l) Analysis of peak intensity variations of (j) and (k) at various annealing temperatures.

exhibits strong preferential orientation, as evidenced by the broad distribution across the entire range except for 54°, suggesting that the solvent itself plays a certain topological role. In the two-step method, the intermediate phase involving NMP is identified as $PbI_2{\cdot}0.5DMF{\cdot}0.5NMP$,[23] differing from the $PbI_2{\cdot}NMP$ intermediate phase observed in the one-step method. This difference can be attributed to the absence of an antisolvent washing step in the two-step process, allowing a significant amount of DMF to be retained and incorporated into the intermediate phase formation. Upon introducing organic ammonium salts in the second step, $PbI_2{\cdot}0.5DMF{\cdot}0.5NMP$ undergoes transformation into $MA_2(DMF)_2Pb_3I_8$, as illustrated in Fig. S14–S16. The (020) plane of the $PbI_2{\cdot}0.5DMF{\cdot}0.5NMP$ intermediate phase exhibits an XRD peak at approximately 8.1°, which is close to that of the (020) planes of $MA_2(DMF)_2Pb_3I_8$, suggesting a topological relationship between the two phases. This implies that $PbI_2{\cdot}0.5DMF{\cdot}0.5NMP$ can act as a crystal growth template for $MA_2(DMF)_2Pb_3I_8$. The formation of $MA_2(DMF)_2Pb_3I_8$ is likely driven by both the introduction of organic ammonium salts (MA^+) and the assistance of NMP. Firstly, with a boiling point of 203 °C (Table S1), NMP does not evaporate completely during annealing, facilitating the formation of the $PbI_2{\cdot}0.5DMF{\cdot}0.5NMP$ intermediate phase. Secondly, the (020) planes of $MA_2(DMF)_2Pb_3I_8$ align with those of $PbI_2{\cdot}0.5DMF{\cdot}0.5NMP$, thereby stabilizing a coherent interface and ultimately promoting the (100) orientation (Fig. 2d).

The topochemical assembly mechanism is considered only one contributing factor of solvent regulation; another critical factor lies in the differential coordination capabilities between solvent molecules and perovskite species.[24] Using the DMF/DMSO solvent system, the XRD intensity variations of PbI_2 and perovskite (111) peaks at gradient temperatures were analyzed. The inconsistent trends between these peaks suggest that in addition to PbI_2 acting as a topological growth template providing driving forces, an unknown interfering factor—specifically the interaction between DMSO and PbI_2—is involved. For instance, the weak and broad peaks of $PbI_2{\cdot}DMSO$, resulting from the strong DMSO–PbI_2 affinity,[25] are highly sensitive to PbI_2 film quality and subsequent organic ammonium salt intercalation, thereby impeding facet growth. This explains why conventional two-step methods using DMF/DMSO solvents typically exhibit poor perovskite crystal growth (often labeled as "control" in the literature) and fail to achieve well-defined crystallographic orientations.[26] The heavy reliance of perovskite crystallization on PbI_2 templates and organic salt infiltration leads to disordered grain formation and unintended defects. Noteworthily, the (111) orientation is attributed to PbI_2 rather than $PbI_2{\cdot}DMSO$. At annealing temperatures above 90 °C, XRD patterns lack peaks for $PbI_2{\cdot}DMSO$, yet the (111) peak remains dominant.

Similarly, in the DMF/NMP solvent system, the intensity variations of the $PbI_2{\cdot}0.5DMF{\cdot}0.5NMP$ intermediate phase and perovskite (100) peaks at gradient temperatures were analyzed. While their trends broadly align, a contradiction arises: even when the intermediate phase is nearly absent at high temperatures, the (100) peak intensity remains the highest. Compared to DMSO, NMP demonstrates stronger affinity for FAI than PbI_2 (Fig. 2i), enhancing organic salt penetration, accelerating intramolecular exchange, and favoring the thermodynamically stable low-surface-energy (100) facet.[27,28] This accounts for the persistence of the dominant (100) facet. Additional analysis of PbI_2 and perovskite (111) peak variations in the DMF/NMP solvents confirms the maintained relationship $(111)_{FAPbI_3}//(001)_{PbI_2}$, which competes with $(100)_{FAPbI_3}//(020)_{PbI_2\,0.5DMF\,0.5NMP}$, ultimately deviating from expected orientations. (Prior studies on the DMF/DMSO/NMP ternary solvent system revealed competing mechanisms between $PbI_2{\cdot}DMSO$ and $PbI_2{\cdot}0.5DMF{\cdot}0.5NMP$ that preclude coexistence, consistent with different solvent regulation. Thus, ternary solvents are excluded here).

Understanding the mechanism of additive influence on orientation

There are various modes of interaction and reaction between additives and perovskites. To determine which mechanism contributes to the observed enhancement by SACR, SEM analysis is conducted to examine changes at the contact interface. As shown in Fig. 3a, under non-annealed conditions, the DMF/DMSO film treated with CHA exhibits tightly connected grains across the entire surface. In contrast, the DMF/NMP film treated with CHAI shows island-like grains without merging into a uniform surface. This distinction highlights the differences between the two additives—CHA penetrates downward and integrates with the perovskite framework, whereas CHAI remains confined at the grain boundaries, acting as a static adsorbate. SEM also confirms that surface treatment prior to annealing can effectively participate in the crystallization process and regulate the orientation.

Theoretical calculations indicate that for the selected additives, CHA and CHAI, the adsorption energies on the (100) facets are both greater than those on the (111) facets, $|E_{ads}\text{-}(100)| > |E_{ads}\text{-}(111)|$ (Fig. 3e and Fig. S21). The results confirm that both CHA and CHAI selectively adsorb onto (100) facets, reducing the surface energy of the (100) planes, thereby promoting (100) orientation. However, CHA does not exhibit this behavior on the (100) orientation, suggesting that the active participant is not CHA itself but another species. This difference is attributed to their distinct chemical properties—one being an amine and the other an ammonium salt. CHA, with its $-NH_2$ tail group, reacts with formamidinium (FA^+) during the SACR process, forming the new cation cyclohexyl formamidinium ($CHAFA^+$), as illustrated in Fig. 3b.

^1H NMR spectroscopy was conducted on the precursor ink to determine whether chemical reactions occur between FA^+ and CHA in solution and to identify the resulting products. In Fig. S25 and S26, the spectra of FAI, CHA, and CHAI are compared. The analysis of Fig. S27 reveals a new species displaying a singlet peak in the ^1H NMR spectrum at a chemical shift (δ) of 7.87 ppm, which is close to the methine resonance of FA^+ (7.80 ppm). Additionally, the ^{13}C NMR spectrum of the same solution exhibits a new signal at 152.21 ppm, indicating the presence of a new methine environment distinct from FA^+.

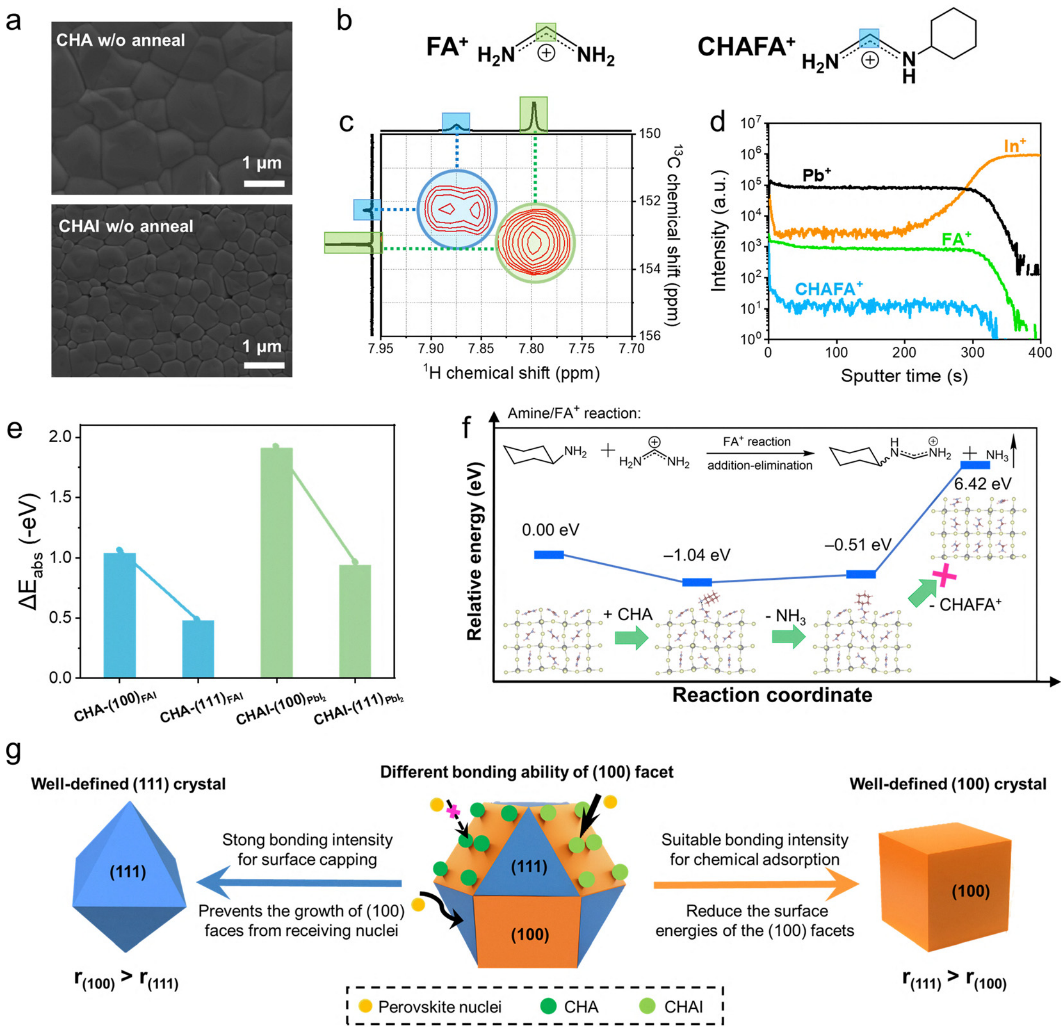

Fig. 3 (a) SEM images of thin films after SACR treatment without annealing. (b) Schematic diagram of the ^1H signal positions for FA^+ and $CHAFA^+$. (c) 2D ^1H–^{13}C NMR spectrum of the CHA and FAI reaction mixture in DMSO-d_6. (d) TOF-SIMS molecular distribution of perovskite film with 0.2 mol% of CHA additive. (e) Adsorption energy on the (100) and (111) facets for each additive. (f) Energy variation and the corresponding reaction scheme of CHA with FA^+. (g) Schematic illustration of crystal facet control using selective capping agents with varying bonding strengths, correlated with the Wulff construction rule.

^1H–^{13}C heteronuclear correlation (HETCOR) NMR spectroscopy confirms that these two new signals correspond to bonded nuclei in Fig. 3c.[30,31] These results are consistent with the formation of $CHAFA^+$ through the nucleophilic attack of CHA on FA^+, followed by the elimination of NH_3. Fig. 3d presents time-of-flight secondary ion mass spectrometry (TOF-SIMS) data obtained after introducing CHA into $FAPbI_3$ films, where the detected $CHAFA^+$ (m/z = 127) peaks confirm that the reaction occurs.

As shown in Fig. 3f, the formation of $CHAFA^+$ was modeled on the FAI-terminated (100) surface, given that CHA can readily access FA^+. The adsorption energy of CHA on the studied surface is −1.04 eV, which suggests that the reaction between CHA and FA^+ is highly probable. The formation of $CHAFA^+$ with the release of NH_3 is a slightly endothermic process, with a reaction energy of 0.53 eV. The desorption of $CHAFA^+$ from the surface is a highly unfavorable process, meaning that $CHAFA^+$ works as a surface capping agent. The $CHAFA^+$ modification has the potential to impede the cation exchange between the $FAPbI_3$ monomer and the existing crystal facets, thereby inhibiting the growth of the (100) facets and limiting the mass transport to the (100) facets.[32] In contrast, the CHAI additive functions solely as an interfacial passivant, exhibiting a selective tendency to cover the (100) facets, reduce the surface energies of the adsorbed facets, and slow down their growth rate.[33] This ultimately increases the percentage of exposed (100) facets on the overall crystal surface.[34] The key difference between CHA and CHAI lies in the varying chemical bond strengths between different additives and the crystal nucleus facets.

Similar evidence can be observed in the PFs. By comparing the experimental PFs with the Wulff stereographic projections[35] for a single crystal perfectly aligned along the [111] (in brown) and [100] (in orange) crystallographic directions, the mechanism of (111) and (100) orientation with different additives was investigated (Fig. S32). The strong peak at the center of PF (111) for the DMF/DMSO film confirms preferential growth along the [111] direction, where crystals tend to grow horizontally to the substrate, consistent with the GIWAXS results. Similarly, the central peak of PF (100) for the DMF/NMP film confirms the horizontal orientation of (100) planes. However, the PF variations of the non-dominant crystal plane for each solvent system differ. The central peak of PF (100) for the DMF/DMSO film shifts towards the Φ = 54.7° diffraction ring. Conversely, the central diffraction ring of PF (111) for the DMF/NMP film remains nearly unchanged. This indicates that the additive influences the (100) plane rather than the (111) plane.

Building on previous findings, two driving forces behind the SACR of different facets were identified: solvents and additives. Since a homogeneous orientation could not be achieved by merely exchanging additives in two solvent systems, it is suggested that solvent regulation, through the formation of topological templates (or intermediates), serves as the initial driving force to induce the preferential growth of a specific crystal facet. Subsequently, the corresponding additive lowers the activation energy of precursor ion transport, acting as a secondary driving force to achieve orientation homogeneity. The anisotropic adsorption behavior of additives ultimately transforms facet heterogeneity into homogeneity. Inspired by the Wulff construction rule[36] used in the catalytic synthesis of high-index faceted nanocrystals, the growth processes of the respective crystal facets can be mapped out (Fig. S33).

Analysis facet-dependent properties

The perovskite films with distinct crystallographic orientations were systematically investigated using atomic force microscopy (AFM), Kelvin probe force microscopy (KPFM), and confocal photoluminescence (PL) mapping (Fig. 4). Here, due to the more random orientation of films prepared in DMF/DMSO compared to that in DMF/NMP, the former without SACR was chosen as the control random-oriented sample. After SACR treatment, morphological evolution was initially characterized through AFM imaging (Fig. 4a and Fig. S35), revealing average surface roughness values of 29.7 nm, 27.9 nm, and 23.0 nm for random-, (111)-, and (100)-oriented films, respectively, across 5 × 5 μm^2 scan areas. The AFM height difference distribution

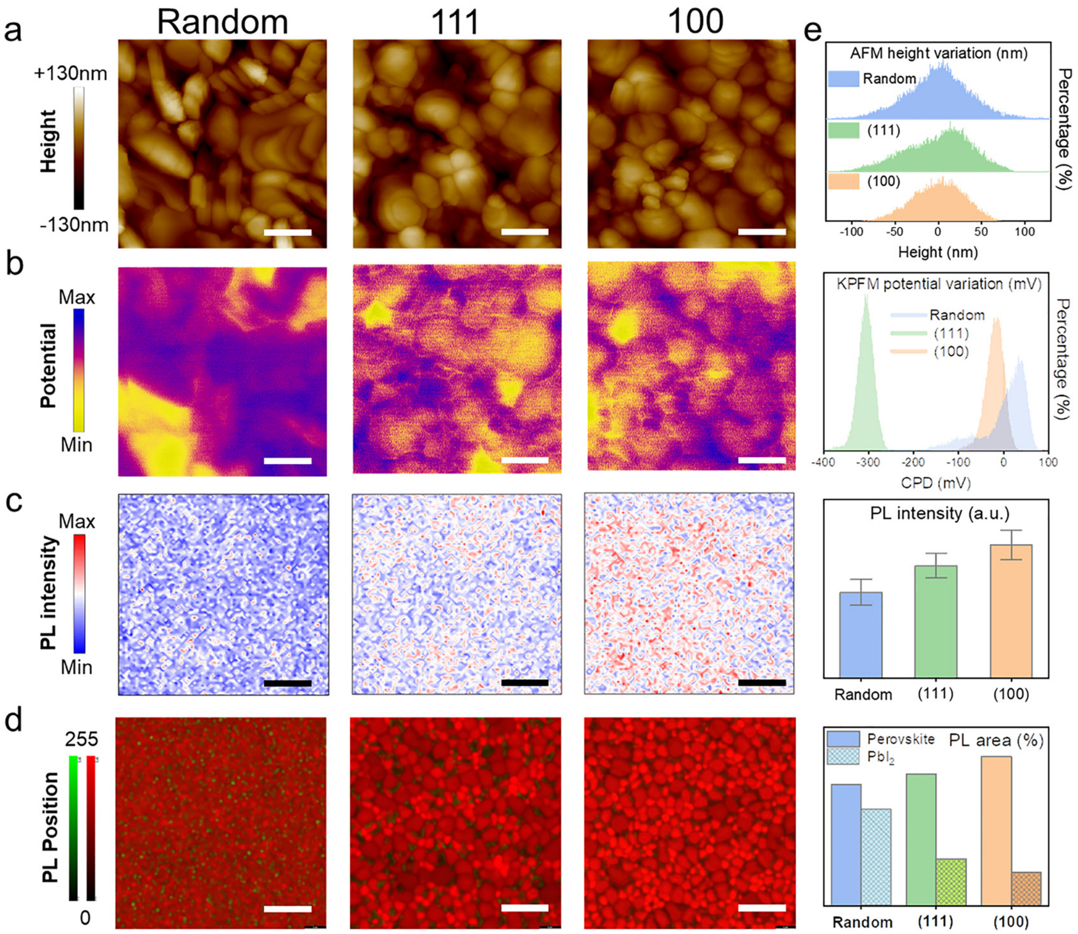

Fig. 4 Various perovskite films with different orientations visualized by AEM (scale bars, 1 μm) (a), KPFM (scale bars, 1 μm) (b), confocal PL-intensity mapping (scale bars, 20 μm) (c) and confocal PL-position mapping (scale bars, 5 μm) (d). (e) A visualization summary of the perovskite films by using the respective characteristic parameters of different visualization methods.

exhibits progressive concentration, aligning with the transition from heterogeneity to homogeneity. The asymmetric height distribution observed in (111)-oriented films originated from the triangular geometry of the (111) facet, contrasting with the lateral structure of the (100) facet.

KPFM images demonstrate analogous consistent trends. Both (100)- and (111)-oriented films exhibited more uniform contact potential difference (CPD) distributions with less fluctuations, compared to random-oriented films (Fig. 4b), facilitating effective carrier extraction and stable device operation. Notably, the (111)-oriented films demonstrated superior surface potential homogeneity despite greater morphological variations, suggesting enhanced operational stability against external electrical bias conditions. Surface potential shifts were systematically recorded, with (111)-oriented facets displaying characteristic negative shifts (p-type behavior) and (100)-oriented facets showing positive shifts (n-type behavior), consistent with their intrinsic energy level offsets as referenced in prior studies.[37] This facet-dependent electronic behavior directly correlates with carrier extraction efficiency. Since this work employs a surface treatment approach before annealing, the surface energetics are indeed influenced not only by orientation control but also by additive-induced defect passivation. For example, the reaction between CHA and FAI results in PbI_2 termination at the surface, which favors p-type character, while CHAI plays a passivation role by reducing the influence of exposed halogens on the n-type character.

Confocal PL-intensity mapping measurements were conducted across an extended $100 \times 100\ \mu m^2$ scan area for the same perovskite film series. Fig. 4c also reveals a progressive enhancement in overall PL intensity with improved uniformity across oriented films, whereas the most prevalent were observed on the random film. This phenomenon is attributed to localized defect degradation and interfacial heterogeneity, correlating with morphological features identified in prior analyses. (100)-oriented films demonstrated superior carrier transport capabilities.

Localized surface analysis probed PbI_2 and perovskite emission bands simultaneously, with superimposed position mappings (Fig. 4d). PL-position distributions demonstrated consistency with intensity profiles. The PL-position mappings are consistent with the PL-intensity mappings. On both the μm^2- and hundreds of μm^2-scale, the homogeneous oriented-perovskite film shows more uniform PL intensity distributions. In the PL-position mappings, the perovskite grains exhibited exclusive red emission, whereas the PbI_2 clusters showed green emission, corresponding to PL signals collected in the 750–850 nm and 450–600 nm windows, respectively. In the random film, PbI_2 accumulates at grain boundaries, causing poor HTL contact. After SACR treatment, PbI_2 becomes finely dispersed, leading to improved interface morphology in Fig. S41 and S42. SACR treatment effectively modulated PbI_2 distribution across all films, while the (100)-oriented film exhibits minimal residual PbI_2—a critical factor enhancing charge transport efficiency that potentially contributes to their superior PL performance.

It is undeniable that the additive provides a defect-passivation effect, which enhances the facet-dependent properties. Although defect passivation and orientation regulation cannot be fully decoupled, the results in Fig. S43 could indicate that orientation regulation is the dominant factor.

Device performance and stability

PSCs with a device configuration of ITO/SnO_2/Perovskite/Spiro-OMeTAD/Au (Fig. S44) have been fabricated for different orientations. Detailed methods are in the SI. PCE histograms (Fig. 5b and c) show that random-oriented PSCs have an average PCE of 19.66%. The uniform single (111) orientation increases the average PCE to 22.53%, while the (100) orientation boosts it to 24.62%, with the best PCE exceeding 25%. The highest PCE of 25.33% is achieved by the (100) single orientation solar cell, compared to 23.32% for the (111) orientation one. Previous results in Fig. 4c have shown that the (100) facet has a higher photocurrent with higher carrier mobility along the [100] direction, while the (111) facet has a slightly higher defect density, making it suboptimal for PCE.[17,38] The statistical distributions of short-circuit current density (J_{sc}), the open-circuit voltage (V_{oc}), and the fill factor (FF) (Fig. S45) indicate that the higher PCE is due to improvements of all parameters, reflecting enhanced perovskite quality.

The energy level of the perovskite films was further characterized using ultraviolet photoemission spectroscopy (UPS). The work function and valence band maximum (VBM) of perovskite films can be calculated by means of the secondary electron cutoff and valence band spectrum. Based on these data and bandgap, the energy level diagram of the different perovskite films was depicted. As can be seen in Fig. 5d, the (111)-oriented film provides a deeper VBM and conduction band minimum (CBM). Generally, the CBM of perovskites should be slightly higher than the conduction band of the electron transport layer (ETL), and the VBM should be slightly lower than the valence band of the hole transport layer (HTL). This energy level difference forms the built-in electric field that drives charge separation. If the energy level difference is too small, the driving force for charge separation is insufficient, leading to an increased probability of electron–hole recombination; if the energy level difference is too large, although the driving force for separation is enhanced, a potential barrier (such as a Schottky barrier) may form at the interface, hindering carrier transport. Consequently, the (100) structure has more suitable energy level positions between the ETL and the HTL, resulting in more efficient electron transport and extraction. These findings are consistent with the KPFM results in Fig. 4b.

Moreover, the photoluminescence quantum yield (PLQY) was employed to evaluate non-radiative recombination losses, and the quasi-Fermi level splitting (QFLS) was determined. Higher PLQY and QFLS confirm reduced interfacial losses. As shown in Fig. 5e, the perovskite films optimized by the SACR method exhibited increased PLQY and QFLS values compared to those of the randomly oriented film, whether on glass or on the transport layer. For (111)-oriented films, the HTL/perovskite stack is more favorable, while (100)-oriented films benefit from

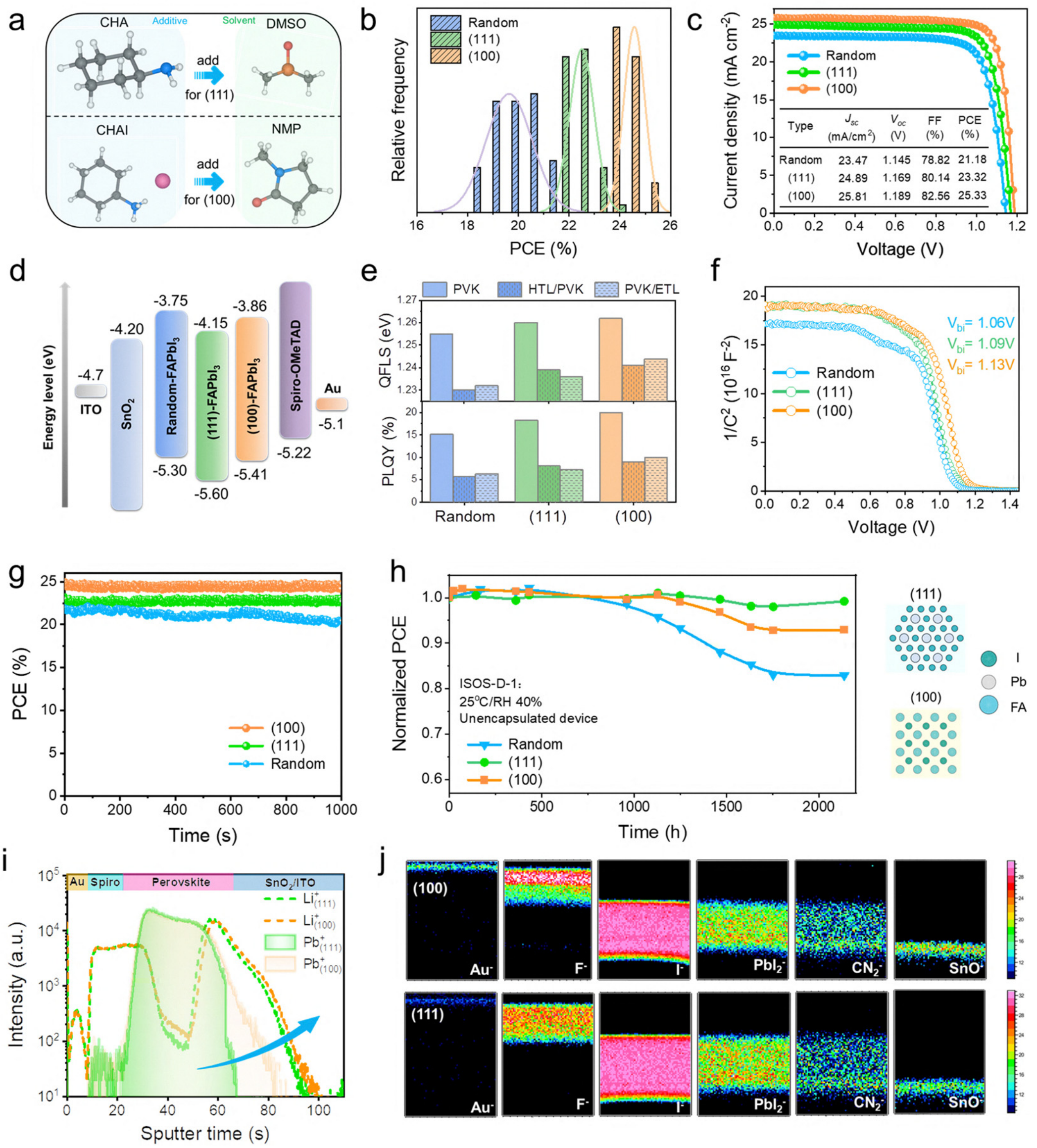

Type	J_{sc} (mA/cm^2)	V_{oc} (V)	FF (%)	PCE (%)
Random	23.47	1.145	78.82	21.18
(111)	24.89	1.169	80.14	23.32
(100)	25.81	1.189	82.56	25.33

Fig. 5 (a) Molecular structure of SACR designs. (b) PCE distribution histograms of the cells with different orientations. (c) J–V curves of the different solar cells and detailed performance parameters statistics. (d) Energy level of each layer in PSCs. The energy level alignment references the vacuum level. (e) Photoluminescence quantum yield (PLQY) measurements and internal quasi-Fermi level splitting (QFLS) diagram for neat perovskite films and at the HTL/perovskite and perovskite/ETL interfaces. (f) Mott–Schottky plots. (g) Steady-state power output of the solar cells for 1000 s. (h) Long-term stability test at an RH of 40% at room temperature. Operational stabilities of PSCs complying with ISOS-L-1 and schematic of atomic arrangements on (111) and (100) crystal facets. (i) TOF-SIMS depth profiles of (100) and (111) perovskite devices in the positive ion mode with Li^+ and Pb^+. (j) TOF-SIMS cross-sectional image of (100) and (111) perovskite devices in the negative ion mode with Au^-, F^-, I^-, PbI_2^-, CN_2^- and SnO^-.

the ETL/perovskite stack, reflecting the p-type nature of (111) and the n-type nature of (100). Furthermore, QFLS provides insight into the open-circuit voltage (V_{oc}) of the solar cell. The variation of the QFLS was calculated based on previous literature (Table S2). The enlargement of QFLS is beneficial for improving V_{oc}, consistent with the enhanced built-in voltages extracted from the Mott–Schottky measurements (Fig. 3g).

Interestingly, the (111) facet presents advantages in terms of stability. We evaluated the effect of facet orientation on the long-term stability of unencapsulated perovskite devices by exposing them to air atmospheres with 40% relative humidity (RH). As shown in Fig. 5h, all the SACR films sample maintains >90% of the initial PCE after 2000 hours, whereas the PCE of the random-oriented device decreases to 83% of the initial value. The long-term stability demonstrates that the (111) orientation is more stable. The stability of the (111) facet originates from its intrinsic properties, including featuring closely packed atoms with higher bond energies, making it more resistant to moisture-induced corrosion.[39] The difference in the atomic ratios is exposed on the two crystal facets, and thus (111)-oriented films demonstrate excellent humidity stability. Although the (111) facet is densely packed, perovskite is an ionic crystal rather than a structure with closely packed atoms. Instead, it features the arrangement of ions such as FA^+ and PbI_3^-. Under an external bias, this packing makes it susceptible to layer stacking faults and ion migration, which is one reason for the higher defect density on the (111) facet. The introduced CHA effectively addresses the issues caused by the ionic lattice through strong interactions and steric hindrance, thereby better reflecting the intrinsic stability of the (111) facet. Simultaneously, the formation of large cations $CHAFA^+$ isolates the facet from chemical interactions with environmental O_2/H_2O molecules, effectively mitigating the adverse effects of ambient moisture on the perovskite crystal framework. This further enhances the stability of the perovskite. It is acknowledged that defect passivation contributes to performance enhancement, but this effect can only be qualitatively assessed rather than quantitatively distinguished at present.

The (111)-oriented films also demonstrate exceptional suppression of ion migration. The TOF-SIMS depth profiles (Fig. 5i), cross-section images (Fig. 5j), and three-dimensional and two-dimensional images (Fig. S62–S64) confirm the uniform distribution of elements within the bulk of the homogeneous-oriented films. Specifically, the elemental distribution in the (111)-oriented films is more uniform than in the (100)-oriented films, where ion migration or accumulation is evident at the interfaces. This occurs because the low-boiling-point CHA evaporates from the film during the annealing process, spontaneously migrating from the bottom to the top and preventing compositional disorder. Moreover, due to the unique chair-shaped conformation of CHA, there is significant steric hindrance at the grain boundaries, which inhibits ion migration. Halide migration occurs not only between adjacent octahedral structures but also within individual octahedra. Only CHA can effectively inhibit both types of migration by interacting with FA^+ ions at the perovskite surface, while CHAI, as a surface passivation agent, can only suppress the former. Additionally, the zipper-type lattice distribution of (111)-oriented films facilitates denser packing, which helps to inhibit ion migration—an attribute not found in (100)-oriented films. Consequently, SEM images reveal that (111)-oriented films exhibit better stacking, with a clean buried interface and no voids at the interface with ITO, in stark contrast to the other oriented films (Fig. S65).

Conclusions

This work establishes a novel solvent-additive cascade regulation (SACR) strategy to achieve homogeneous facet engineering in perovskite solar cells (PSCs), resolving long-standing challenges in fabricating high-quality, orientation-tunable crystal facets. By synergistically integrating solvent-mediated topochemical assembly and additive-regulated facet-selective growth, the SACR method enables the controlled synthesis of homogeneous (111)- and (100)-oriented perovskite films governed by Wulff construction principles. Mechanistic investigations reveal two-stage crystallization dynamics: (i) PbI_2 or $PbI_2 \cdot 0.5DMF \cdot 0.5NMP$ in solvent systems (DMF/DMSO or DMF/NMP, respectively) that dictate primary facet orientation by topochemical assembly, while (ii) additives (CHA/CHAI) modulate facet evolution through facet-dependent bonding interactions and mass transfer kinetics. Specifically, CHA penetrates the perovskite lattice, where its $-NH_2$ group undergoes nucleophilic substitution with FA^+ to form cyclohexylformamidinium ($CHAFA^+$), which anchors onto the (100) facets. Acting as a strong end-capping agent, $CHAFA^+$ suppresses the growth of the (100) facets, thereby indirectly promoting (111) orientation. In contrast, CHAI serves as a surface adsorbate on the (100) facets, reducing their surface energy *via* electrostatic interactions and directly facilitating the (100) orientation.

The resulting (100)-oriented n–i–p structured devices achieved a notable efficiency of 25.33%, attributed to efficient carrier extraction and suppressed carrier recombination, whereas (111)-oriented counterparts exhibited exceptional operational stability (>95% PCE retention after 2000 h) due to enhanced environmental resistance. Crucially, this work decouples the distinct roles of solvents (orientation initiation) and additives (facet refinement), providing a universal framework for crystal engineering. By correlating facet-dependent electronic properties with device performance metrics, the findings advance the fundamental understanding of perovskite crystallization thermodynamics while establishing scalable protocols for tailoring optoelectronic materials *via* orientation control.

Conflicts of interest

The authors declare no conflicts of interest.

Data availability

All data are available in the main text or the supplementary information (SI). Supplementary information: device fabrication and characterization techniques, including TEM, SEM, *J–V*, KPFM, NMR, EQE, FTIR, UV–vis, XRD, pole figures, inverse pole figures (IPF), orientation distribution function (ODF), GIWAX, PL mapping, PLQY, TOF-SIM, and Nyquist plots; the experimental results (Fig. S1–S65), including diffraction pattern; *J–V* curves of PSCs; distribution of PV parameters of PSCs; stability test; DFT results, and Tables S1–S3 detailed photovoltaic parameters of different condition PSCs based on champion devices; the PLQY and calculated QFLS with different device stacks; fitted TRPL parameters (PDF). See DOI: **https://doi.org/10.1039/d5ee04415d**.

Acknowledgements

This work was supported by the Strategic Priority Research Program of the Chinese Academy of Sciences (Grant No. XDB1140101). This work was conducted by the Fundamental Research Center of Artificial Photosynthesis (FReCAP), supported by DICP (Grant: DICP I202469), financially supported through the National Natural Science Foundation of China (22088102). Bo Zhou gratefully acknowledges Prof. Jie Su (Xi'an University of Electronic Science and Technology) and Prof. Tongle Bu (Wuhan University of Technology) for their generous sharing of the crystal structure file ($PbI_2·0.5DMF·0.5NMP$.cif). Their collegial support and expertise were invaluable to this work.

References

1 H. Chen, C. Liu, J. Xu, A. Maxwell, W. Zhou, Y. Yang, Q. Zhou, A. S. R. Bati, H. Wan, Z. Wang, L. Zeng, J. Wang, P. Serles, Y. Liu, S. Teale, Y. Liu, M. I. Saidaminov, M. Li, N. Rolston, S. Hoogland, T. Filleter, M. G. Kanatzidis, B. Chen, Z. Ning and E. H. Sargent, Improved Charge Extraction in Inverted Perovskite Solar Cells with Dual-Site-Binding Ligands, *Science*, 2024, **384**(6692), 189–193, DOI: **10.1126/science.adm9474**.

2 L. Zhang, L. Mei, K. Wang, Y. Lv, S. Zhang, Y. Lian, X. Liu, Z. Ma, G. Xiao, Q. Liu, S. Zhai, S. Zhang, G. Liu, L. Yuan, B. Guo, Z. Chen, K. Wei, A. Liu, S. Yue, G. Niu, X. Pan, J. Sun, Y. Hua, W.-Q. Wu, D. Di, B. Zhao, J. Tian, Z. Wang, Y. Yang, L. Chu, M. Yuan, H. Zeng, H.-L. Yip, K. Yan, W. Xu, L. Zhu, W. Zhang, G. Xing, F. Gao and L. Ding, Advances in the Application of Perovskite Materials, *Nano-Micro Lett.*, 2023, **15**(1), 177, DOI: **10.1007/s40820-023-01140-3**.

3 Facet-dependent photovoltaic efficiency variations in single grains of hybrid halide perovskite | Nature Energy. **https://www.nature.com/articles/nenergy201693** (accessed 2024-04-30).

4 S. Shin, S. Seo, S. Jeong, A. S. Sharbirin, J. Kim, H. Ahn, N.-G. Park and H. Shin, Kinetic-Controlled Crystallization of α-FAPbI3 Inducing Preferred Crystallographic Orientation Enhances Photovoltaic Performance, *Adv. Sci.*, 2023, **10**(14), 2300798, DOI: **10.1002/advs.202300798**.

5 X. Liu, Z. Wu, H. Zhong, X. Wang, J. Yang, Z. Zhang, J. Han, D. Oron and H. Lin, Epitaxial 2D PbS Nanosheet-Formamidinium Lead Triiodide Heterostructure Enabling High-Performance Perovskite Solar Cells, *Adv. Funct. Mater.*, 2023, **33**(38), 2304140, DOI: **10.1002/adfm.202304140**.

6 M. Cai, P. Li, J. Ma, Y. Cheng, X. Xu, Z. Ren and Y. Song, The Dominant Roles of the Seed Template in Driving Controllable Growth of Perovskite Crystal, *Nano Today*, 2024, **54**, 102133, DOI: **10.1016/j.nantod.2023.102133**.

7 Z. Fang, N. Yan and S. Liu, (Frank). Modulating Preferred Crystal Orientation for Efficient and Stable Perovskite Solar Cells—From Progress to Perspectives, *InfoMat*, 2022, **4**(10), e12369, DOI: **10.1002/inf2.12369**.

8 C. Wang, B. He, W. Hui, Z. Su, L. Chen, W. Du, L. Zhang, J. Zhang, M. Fu, H. Wang, B. Sun, W. Wen, S. Wang, L. Lou, C. Hou, G. Zheng, L. Song, Y. Chen and X. Gao, Controlling Water for Enhanced Homogeneities in Perovskite Solar Cells with Remarkable Reproducibility, *Adv. Funct. Mater.*, 2024, **34**(41), 2403690, DOI: **10.1002/adfm.202403690**.

9 B. Zhou, P. Zhao, J. Guo, S. Hu, X. Guo, J. Liu and C. Li, Unveiling the Importance of Nondominant Facets in (111)-Dominated Perovskite Films, *ACS Appl. Mater. Interfaces*, 2025, **17**(15), 22715–22726, DOI: **10.1021/acsami.5c01238**.

10 H. Liu, H. Wu, Z. Zhou, L. Ren, Y. Yang, A. Zhang, J. Qian, S. Priya, B. Poudel, C. Liu, D. Yang, K. Wang and C. Wu, Simultaneous Mechanical and Chemical Synthesis of Long-Range-Ordered Perovskites, *Nat. Synth.*, 2025, **4**(2), 196–208, DOI: **10.1038/s44160-024-00687-2**.

11 X. Sun, D. Li, L. Zhao, Y. Zhang, Q. Hu, T. P. Russell, F. Liu, J. Wei and H. Li, 111)-Dominated Perovskite Films by Antisolvent Engineering, *Adv. Mater.*, 2023, **35**(28), 2301115, DOI: **10.1002/adma.202301115**.

12 X. Zheng, Y. Hou, C. Bao, J. Yin, F. Yuan, Z. Huang, K. Song, J. Liu, J. Troughton, N. Gasparini, C. Zhou, Y. Lin, D.-J. Xue, B. Chen, A. K. Johnston, N. Wei, M. N. Hedhili, M. Wei, A. Y. Alsalloum, P. Maity, B. Turedi, C. Yang, D. Baran, T. D. Anthopoulos, Y. Han, Z.-H. Lu, O. F. Mohammed, F. Gao, E. H. Sargent and O. M. Bakr, Managing Grains and Interfaces via Ligand Anchoring Enables 22.3%-Efficiency Inverted Perovskite Solar Cells, *Nat. Energy*, 2020, **5**(2), 131–140, DOI: **10.1038/s41560-019-0538-4**.

13 X. Liu, X. Jiang, Y. Yin, J. Zhang, H. Tian, J. Guo, X. Guo and C. Li, Dominating (111) Facets with Ordered Stacking in Perovskite Films, *Energy Environ. Sci.*, 2024, **17**(16), 6058–6067, DOI: **10.1039/D4EE01863J**.

14 C. Ma, F. T. Eickemeyer, S.-H. Lee, D.-H. Kang, S. J. Kwon, M. Grätzel and N.-G. Park, Unveiling Facet-Dependent Degradation and Facet Engineering for Stable Perovskite Solar Cells, *Science*, 2023, **379**(6628), 173–178, DOI: **10.1126/science.adf3349**.

15 J. Kim, J. Park, J. Lim, J. Kim, J. Kim, N. Shin, J. S. Yun, J. Im and S. Il Seok, Susceptible Organic Cations Enable Stable and Efficient Perovskite Solar Cells, *Joule*, 2025, 101879, DOI: **10.1016/j.joule.2025.101879**.

16 S. Zhang, F. Ma, J. Jiang, Z. Wang, R. T. K. Kwok, Z. Qiu, Z. Zhao, J. W. Y. Lam and B. Z. Tang, Aggregative Luminescence from $CsPbBr_3$ Perovskite Precursors, *Angew. Chem., Int. Ed.*, 2024, **63**(35), e202408586, DOI: **10.1002/anie.202408586**.

17 D. Li, X. Sun, Y. Zhang, Z. Guan, Y. Yue, Q. Wang, L. Zhao, F. Liu, J. Wei and H. Li, Uniaxial-Oriented Perovskite Films with Controllable Orientation, *Adv. Sci.*, 2024, **11**(19), 2401184, DOI: **10.1002/advs.202401184**.

18 K. Pawlik, Determination of the Orientation Distribution Function from Pole Figures in Arbitrarily Defined Cells, *Phys. Status Solidi B*, 1986, **134**(2), 477–483, DOI: **10.1002/pssb.2221340205**.

19 Y.-K. Ahn, Y.-K. Jeong, T.-Y. Kim, J.-U. Cho and N.-M. Hwang, Texture Evolution of Non-Oriented Electrical Steel Analyzed by EBSD and in-Situ XRD during the Phase Transformation from γ to α, *Mater. Today Commun.*, 2020, **25**, 101307, DOI: **10.1016/j.mtcomm.2020.101307**.

20 G. He, T. Peng, B. Jiang, X. Hu, Y. Liu and C. Wu, Recrystallization Behavior and Texture Evolution in Low Carbon Steel during Hot Deformation in Austenite/Ferrite Region, *Steel Res. Int.*, 2021, **92**(10), 2100047, DOI: **10.1002/srin.202100047**.

21 C. Ma, M.-C. Kang, S.-H. Lee, Y. Zhang, D.-H. Kang, W. Yang, P. Zhao, S.-W. Kim, S. J. Kwon, C.-W. Yang, Y. Yang

and N.-G. Park, Facet-Dependent Passivation for Efficient Perovskite Solar Cells, *J. Am. Chem. Soc.*, 2023, **145**(44), 24349–24357, DOI: **10.1021/jacs.3c09327**.

22 C. Zhu, C. Wang, P. Zhang, S. Ma, Y. Chen, Y. Zhang, N. Yang, M. Xiao, X. Cheng, Z. Gao, K. Wen, X. Niu, T. Song, Z. Su, H. Zai, N. Li, Z. Huang, Y. Zhang, H. Wang, H. Zhou, F. Xiao, P. Chen, X. Wang, J. Hong, J. Wang, Y. Bai, X. Gao and Q. Chen, Topochemical Assembly Minimizes Lattice Heterogeneity in Polycrystalline Halide Perovskites, *Joule*, 2023, **7**(10), 2361–2375, DOI: **10.1016/j.joule.2023.08.004**.

23 T. Bu, J. Li, H. Li, C. Tian, J. Su, G. Tong, L. K. Ono, C. Wang, Z. Lin, N. Chai, X.-L. Zhang, J. Chang, J. Lu, J. Zhong, W. Huang, Y. Qi, Y.-B. Cheng and F. Huang, Lead Halide–Templated Crystallization of Methylamine-Free Perovskite for Efficient Photovoltaic Modules, *Science*, 2021, **372**(6548), 1327–1332, DOI: **10.1126/science.abh1035**.

24 J.-W. Lee, Z. Dai, C. Lee, H. M. Lee, T.-H. Han, N. De Marco, O. Lin, C. S. Choi, B. Dunn, J. Koh, D. Di Carlo, J. H. Ko, H. D. Maynard and Y. Yang, Tuning Molecular Interactions for Highly Reproducible and Efficient Formamidinium Perovskite Solar Cells via Adduct Approach, *J. Am. Chem. Soc.*, 2018, **140**(20), 6317–6324, DOI: **10.1021/jacs.8b01037**.

25 Y. Zhang, X. Sun, Z. Guan, D. Li, Q. Wang, Y. Yue, F. Liu, J. Wei and H. Li, Bridging-Solvent Strategy for Quasi-Single-Crystal Perovskite Films and Stable Solar Cells, *Small Methods*, 2025, **9**(1), 2400214, DOI: **10.1002/smtd.202400214**.

26 W. Shao, H. Wang, F. Ye, C. Wang, C. Wang, H. Cui, K. Dong, Y. Ge, T. Wang, W. Ke and G. Fang, Modulation of Nucleation and Crystallization in PbI2 Films Promoting Preferential Perovskite Orientation Growth for Efficient Solar Cells, *Energy Environ. Sci.*, 2023, **16**(1), 252–264, DOI: **10.1039/D2EE03342A**.

27 B. Zhou, P. Zhao, J. Guo, Y. Qiao, S. Hu, X. Guo, J. Liu and C. Li, Unlocking the Potential of Antisolvent-Free Perovskite Solar Cells: Modulating Crystallization and Intermediates through a Binary Volatile Additive Strategy, *Nano Energy*, 2024, **124**, 109487, DOI: **10.1016/j.nanoen.2024.109487**.

28 Y. Li, H. Fan, F. Xu, T. Wang, C. Shan, W. Li, X. Gu, X. Lai, D. Luo, Z. Sun, M. Zhao, X. Li, K. Cui, G. Li and A. K. K. Kyaw, High-Performance Inverted Perovskite Solar Cells Enhanced via Partial Replacement of Dimethyl Sulfoxide with *N*-Methyl-2-Pyrrolidinone, *Sol. RRL*, 2022, **6**(12), 2200816, DOI: **10.1002/solr.202200816**.

29 C. Zhu, C. Wang, P. Zhang, S. Ma, Y. Chen, Y. Zhang, N. Yang, M. Xiao, X. Cheng, Z. Gao, K. Wen, X. Niu, T. Song, Z. Su, H. Zai, N. Li, Z. Huang, Y. Zhang, H. Wang, H. Zhou, F. Xiao, P. Chen, X. Wang, J. Hong, J. Wang, Y. Bai, X. Gao and Q. Chen, Topochemical Assembly Minimizes Lattice Heterogeneity in Polycrystalline Halide Perovskites, *Joule*, 2023, **7**(10), 2361–2375, DOI: **10.1016/j.joule.2023.08.004**.

30 L. Chen, M. Hu, A. M. Risqi, E. Noh, Y. Lee and S. I. Seok, Unraveling the Influence of Solvent on Side Reactions between Formamidinium Lead Triiodide and Methylammonium Cations, *J. Am. Chem. Soc.*, 2024, **146**(14), 10159–10166, DOI: **10.1021/jacs.4c01779**.

31 L. Chen, M. Hu, S. Lee, J. Kim, Z.-Y. Zhao, S.-P. Han, M. S. Lah and S. I. Seok, Deciphering Reaction Products in Formamidine-Based Perovskites with Methylammonium Chloride Additive, *J. Am. Chem. Soc.*, 2023, **145**(50), 27900–27910, DOI: **10.1021/jacs.3c12755**.

32 T.-H. Yang, Y. Shi, A. Janssen and Y. Xia, Surface Capping Agents and Their Roles in Shape-Controlled Synthesis of Colloidal Metal Nanocrystals, *Angew. Chem., Int. Ed.*, 2020, **59**(36), 15378–15401, DOI: **10.1002/anie.201911135**.

33 C. Ran, W. Gao, N. Li, Y. Xia, Q. Li, Z. Wu, H. Zhou, Y. Chen, M. Wang and W. Huang, Facet-Dependent Control of PbI2 Colloids for over 20% Efficient Perovskite Solar Cells, *ACS Energy Lett.*, 2019, **4**(1), 358–367, DOI: **10.1021/acsenergylett.8b02262**.

34 C. Xiao, B.-A. Lu, P. Xue, N. Tian, Z.-Y. Zhou, X. Lin, W.-F. Lin and S.-G. Sun, High-Index-Facet- and High-Surface-Energy Nanocrystals of Metals and Metal Oxides as Highly Efficient Catalysts, *Joule*, 2020, **4**(12), 2562–2598, DOI: **10.1016/j.joule.2020.10.002**.

35 A. Zanetta, V. Larini, Vikram, F. Toniolo, B. Vishal, K. A. Elmestekawy, J. Du, A. Scardina, F. Faini, G. Pica, V. Pirota, M. Pitaro, S. Marras, C. Ding, B. K. Yildirim, M. Babics, E. Ugur, E. Aydin, C.-Q. Ma, F. Doria, M. A. Loi, M. De Bastiani, L. M. Herz, G. Portale, S. De Wolf, M. S. Islam and G. Grancini, Vertically Oriented Low-Dimensional Perovskites for High-Efficiency Wide Band Gap Perovskite Solar Cells, *Nat. Commun.*, 2024, **15**(1), 9069, DOI: **10.1038/s41467-024-53339-6**.

36 C. Wang, Q. Zhang, B. Yan, B. You, J. Zheng, L. Feng, C. Zhang, S. Jiang, W. Chen and S. He, Facet Engineering of Advanced Electrocatalysts Toward Hydrogen/Oxygen Evolution Reactions, *Nano-Micro Lett.*, 2023, **15**(1), 52, DOI: **10.1007/s40820-023-01024-6**.

37 C. Ma, M.-C. Kang, S.-H. Lee, S. J. Kwon, H.-W. Cha, C.-W. Yang and N.-G. Park, Photovoltaically Top-Performing Perovskite Crystal Facets, *Joule*, 2022, **6**(11), 2626–2643, DOI: **10.1016/j.joule.2022.09.012**.

38 C. Ma, M.-C. Kang, S.-H. Lee, S. J. Kwon, H.-W. Cha, C.-W. Yang and N.-G. Park, Photovoltaically Top-Performing Perovskite Crystal Facets, *Joule*, 2022, **6**(11), 2626–2643, DOI: **10.1016/j.joule.2022.09.012**.

39 M. RaeisianAsl, S. Sarabadani Tafreshi and N. H. de Leeuw, A DFT Study of Alkaline Earth Metal-Doped FAPbI3 (111) and (100) Surfaces, *Molecules*, 2023, **28**(1), 372, DOI: **10.3390/molecules28010372**.